Supplementary Information

Dynamically Configurable Hybridization of Plasmon Modes in Nanoring Dimer Arrays

Lei Zhang,[a†] Zhaogang Dong,[b] Ying Min Wang,[b] Yan Jun Liu,[b] Shuang Zhang,[c] Joel Kwang Wei Yang[b,d] and Cheng-Wei Qiu[a,e†]

[a]Department of Electrical and Computer Engineering, National University of Singapore, Singapore 117583, Singapore.

[b]Institute of Materials Research and Engineering, Agency for Science, Technology and Research (A*STAR), Singapore 117602, Singapore.

[c]School of Physics & Astronomy, University of Birmingham, Birmingham B15 2TT, UK.

[d]Singapore University of Technology and Design, Singapore 138682, Singapore.

[e]SZU-NUS Collaborative Innovation Center for Optoelectronic Science & Technology, Shenzhen University, Guangdong 518060, China.

[†]Corresponding email: elezlei@nus.edu.sg or eleqc@nus.edu.sg

1. Method

Simulation: The commercial finite–difference time–domain (FDTD) code from LUMERICAL was used to simulate the transmittance and field distributions. A plane wave was normally incident on the proposed structures under different polarizations. Periodic boundary conditions were used along *x*- and *y*-axis and perfect matched layer (PML) was used along *z*-axis. The refractive index of SiO_2 was set to be 1.45. The permittivity of Au was taken from experimental data.[1]

Sample fabrication: The sample was fabricated on a BK7 glass substrate. To avoid the charging problem during EBL (Elionix ELS-7000) process, 3-nm-Cr was evaporated onto the glass substrate using electron-beam evaporator (Denton Explorer) with a pressure of 10^{-7} torr and an evaporation rate of 0.2 Å/s. Moreover, additional 100 nm of SiO_2 was evaporated on top of Cr as a dielectric spacer to reduce the plasmon damping loss. Polymethyl methacrylate (PMMA, 950k molecular weight) resist with a concentration of 2.5% wt. in anisole was then spin-coated onto the glass substrate and the resist thickness was around 100 nm. The sample was baked at 180 ^{o}C for 2

minutes for reducing the residual stress and removing the solvent in PMMA resist. During EBL, the electron acceleration voltage, beam current and exposure dwell time were 100 KeV, 100 pA, and 1.05 µs, respectively. After the exposure, the sample was developed using a methyl isobutyl ketone/isopropyl alcohol (MIBK/IPA, volume mixing ratio of 1:3) at 0 ^{o}C for 15 seconds. The sample was then deposited with 1-nm-Ti and 40-nm-Au using electron-beam evaporation at a pressure of 10^{-7} torr and a deposition rate of 0.2 Å/s. Lift-off was done by immersing the sample in 70 ^{o}C N-methyl-2-pyrrolidone (NMP) solution. After the lift-off process, the sample was cleaned using Acetone, IPA and dried with a continuous flow of nitrogen.

Optical characterization: The transmission optical spectra were obtained with a spectrograph (Princeton Instruments, Acton SP 2300) and a thermoelectrically cooled InGaAs detector (Acton Research Corporation, ID-441-C) attached to an inverted optical microscope (Olympus, IX81). Light from a halogen lamp was passed through a near-infrared polarizer and then focused onto the sample using a light condenser with NA = 0.2. The transmitted light was collected by a 60× objective lens and directed to the spectrograph. The transmittance measurements obtained were normalized with respect to the sample substrate.

2. Mode supported by single nanoring

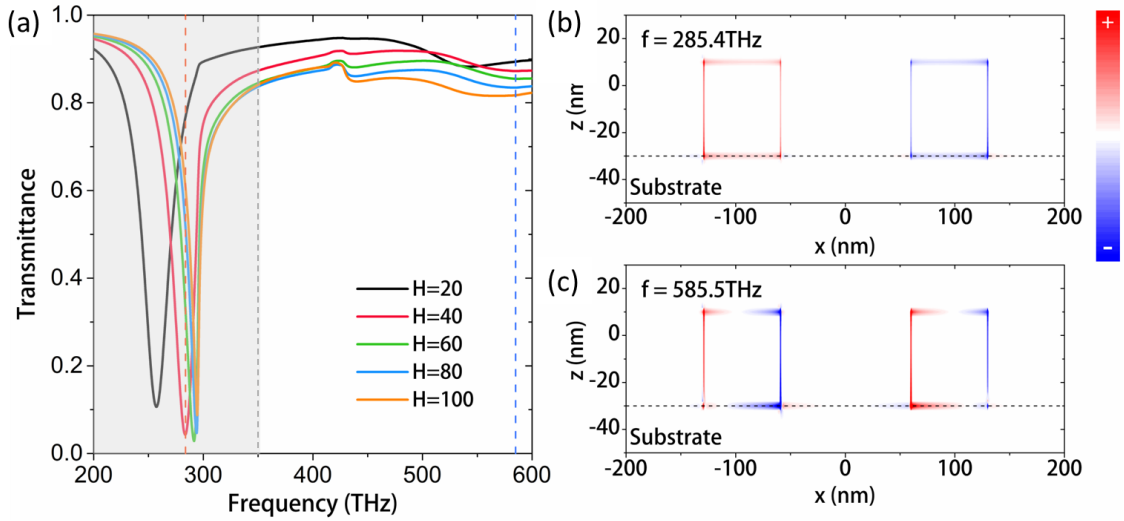

Fig. S1 (a) Transmittance evolution of single nanoring supporting dipolar mode by increasing height of nanoring from 20 nm to 100 nm. Other parameters are the same as used in the main text. (b) Charge distribution of bonding mode at low frequency (285.4THz) labeled by red dashed line in (a). (c) Charge distribution of anti-bonding mode at high frequency (585.5THz) labeled by blue dashed line in (a). Both charge distributions are calculated with H = 40 nm.

The resonant modes of single nanoring arise from two types of coupling, including the coupling of the inner and outer walls, and top and bottom surfaces. As shown in Fig. S1a, two transmission dips are observed. The dip at low frequency is sharp and deep due to efficient interaction with incidence while the dip at high frequency is hard to be identified due to minute interaction.

3. Transmittance spectrum of single nanoring

In main text, the size of nanoring supporting quadruplar mode is determined by the aligning transmission peak with transmission dip as shown in Fig. S2a. In order to estimate the full-width half-maximum (FWHM), quadruplar mode is excited under inclined incidence at angle 30°. However, due to retardation effect, the resonance frequency is slightly larger.

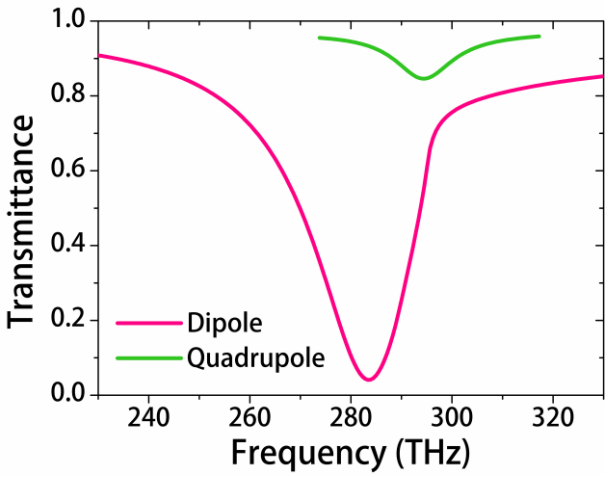

Fig. S2 Transmittance spectra supported by single nanoring. Dipolar mode is excited under normally incident light while quadruplar mode is excited under inclined incidence at angle 30°.

4. Comparison of transmittance spectra simulated under different illumination angles

Incident angle may be another way to tuning the PIT effect on certain structures with strong angle-dependent resonances. Nevertheless, this angle tuning effect might be weak on the proposed asymmetric dimer nanoring structure here. As shown in Fig. S3(a), when polarization angle $\varphi = 0^{o}$, the transparency peak exists a blue shift as the incident angle θ is increased from 0^{o} to 30^{o}. Although the transmittance of peak value gets larger at $\theta = 30^{o}$, the modulation depth is only 37% at 291 THz due to the high transmittance at the corresponding frequency when $\varphi = 90^{o}$. As the transmittance

spectra of single nanorings shown in Fig. S3(b), the frequencies of both dipolar and quadrupolar modes blue-shift as θ increases. However, different shift amounts weaken their coupling strength. Therefore, incident angle tuning effect is not obvious on the dimer nanoring structures.

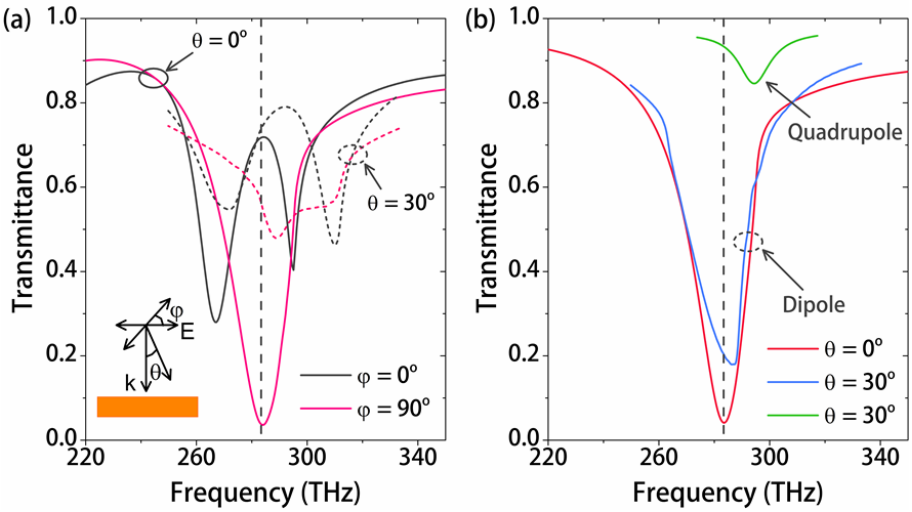

Fig. S3 Comparison of transmittance spectra of (a) dimer nanoring and (b) single nanoring under different illumination angles.

5. Diffraction coupling in the proposed nanoring dimer system

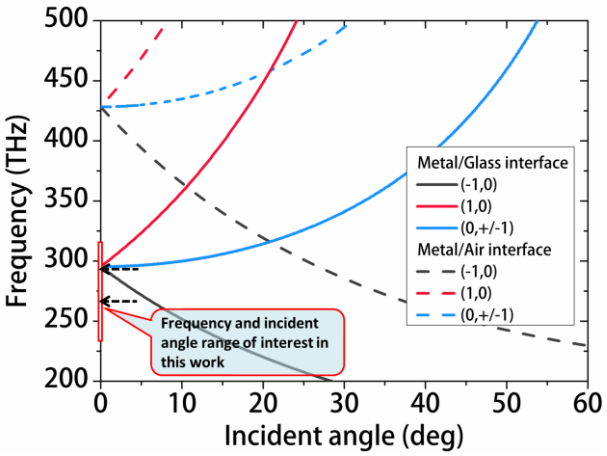

Fig. S4 Dispersion relation at metal/glass (solid lines) and metal/air (dashed lines) interfaces, respectively. The frequency of interest ranges from 220 THz to 330 THz, while the incident angle θ_i is 0 in this work. Two black arrows represent the resonance frequency of the hybridized modes.

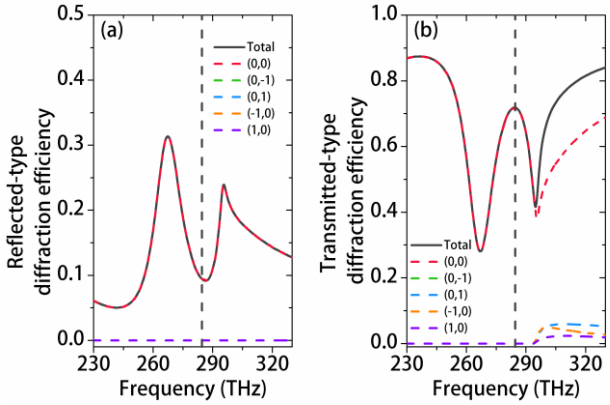

Fig. S5 Diffraction efficiency at reflection (a) and transmission (b) spaces, respectively.

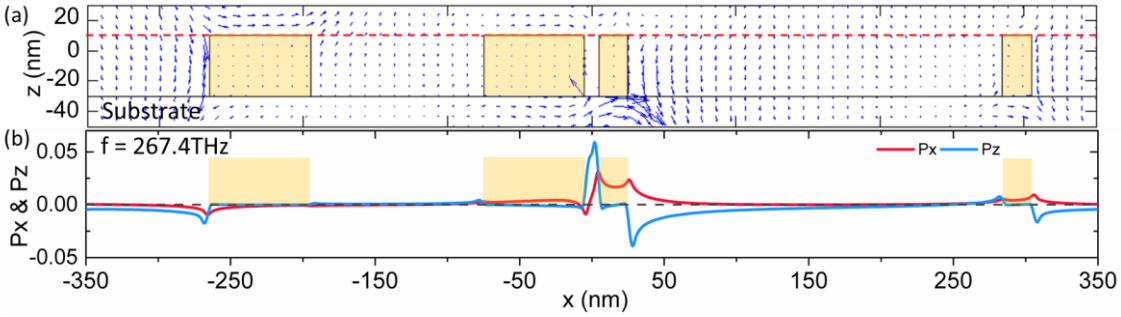

Fig. S6 Poynting vector in one unit cell at y=0 plane for f = 294.5 THz. (a) The combination of Px and Pz components shows that energy flow downwards at the boundary of unit cell. (b) Px and Pz components are plotted separately at the surface plane of nanoring, indicated by the red dashed in line in (a). Light yellow areas represent the cross section of nanorings.

In previous studies, sharp resonance of periodic nanoparticle array benefits from the diffraction coupling. In contrast, our case is quite different from those works. Diffraction coupling can only take place when the momentum is matched by the diffraction equation, $\vec{k}_d = k_0 \sin\theta_i \hat{x} + m\frac{2\pi}{P}\hat{x} + n\frac{2\pi}{P}\hat{y}$, where $\vec{k}_d$ is the wave vector of diffracted light, k_0=2π/λ is the wave vector of incidence in vacuum, θ_i is the incident angle, *P* is the periodicity of grating, integer *m* and *n* are diffraction orders, $\hat{x}$ and $\hat{y}$ are unit vector along *x*- and *y*-axis, respectively.

In order to exclude the influence of diffraction coupling, the periodicity is selected to be 700 nm (428.3 THz), which is far away from the resonance wavelengths of hybridized modes 1018 nm (294.5 THz) and 1121 nm (267.4 THz). As shown in Fig. S3, the diffraction equation cannot be fulfilled at metal/air interface (dashed lines) in the frequency range of interest at normal incidence (i.e. φ = 0°). As a result, no energy is channeled into higher diffraction orders, which further verifies that no

diffraction coupling takes place in reflected light, as shown in Fig. S5a. On the other hand, transmitted light with frequency larger than 294.7 THz could be diffracted at the metal/glass interface. As shown in Fig. S5b, tiny part of energy of high frequency hybridized mode is channeled into higher diffraction orders (0, +/-1) and (+/-1, 0). The diffraction efficiency of each high order mode is less than 5% while the total diffraction efficiency of high order modes is less than 18% at the frequency larger than 294.7 THz. Therefore, the narrow linewidth slightly results from the diffraction coupling. However, it is evident that all the transmitted energy goes into (0, 0) order at low frequency hybridized mode at 267.4 THz. There is no diffraction coupling involved in this mode. Notably, the linewidth (16.6 THz) of the low frequency hybridized mode is still narrower than the theoretical Drude limit (18 THz). Therefore, such narrow linewidth should be attributed to the localized coupling between bright and dark modes rather than diffraction coupling. As a further justification, the Poynting vector at y = 0 plane is plotted at frequency 267.4 THz in Fig. S6. It is clear that x-component of Poynting vector Px is equal to zero at the boundaries of the unit cell. In Fig. S6b, Px is zero and Pz is negative, which mean that energy flows downward at the surface of structures rather than into neighboring unit cells.

In conclusion, although diffraction coupling slightly contributes to the narrow linewidth of high frequency hybridized mode, localized coupling within one unit is the main reason to generate a sharp resonance with linewidth narrower than the theoretical Drude limit of Rayleigh particles.

6. The coupled Lorentz oscillator model and parameters fitting

One oscillator of amplitude A_1 denotes the superradiant mode, which can interact with incoming light directly with a geometric factor η. The other oscillator of amplitude A_2 denotes the subradiant mode, which cannot be excited directly by the incoming light due to the lack of a net dipole moment. However, it can be excited through near-field coupling with a coupling strength of κ. The coupled equations can be expressed as follows: [2-4]

$$\begin{pmatrix} -\omega+\omega_1-i\gamma_1/2 & -\kappa \\ -\kappa & -\omega+\omega_2-i\gamma_2/2 \end{pmatrix}\begin{pmatrix} A_1 \\ A_2 \end{pmatrix}=\begin{pmatrix} \eta E_0 \\ 0 \end{pmatrix} \quad (1)$$

where γ_j is the damping rate. E_0 is the amplitude of incident field. Since the incident energy is not perfectly coupled into the superradiant dipole mode, a constant field component *bg* should be taken into account as a background.[5-7] By solving eqn (1), the amplitude of superradiant mode can be obtained as:

$$|A_1| = \left| \frac{\eta(-\omega+\omega_2-i\gamma_2/2)}{(-\omega+\omega_1-i\gamma_1/2)(-\omega+\omega_2-i\gamma_2/2)-\kappa^2} E_0 + bg \right| \quad (2)$$

Under different polarizations, the field nodes of the dipolar mode rotate accordingly. Therefore, the field magnitudes for different polarizations are extracted from different locations 5 nm apart from the left nanoring supporting superradiant mode with a coordinate of (x, y) = (-((d_1/2 + 5 nm) cosφ + x_1), -(d_1/2 + 5 nm) sinφ + y_1), where (x_1, y_1) = (-135 nm, 0) is the center coordinate of the left nanoring and d_1 = 260 nm. The fit curves are plotted in Fig. S7.

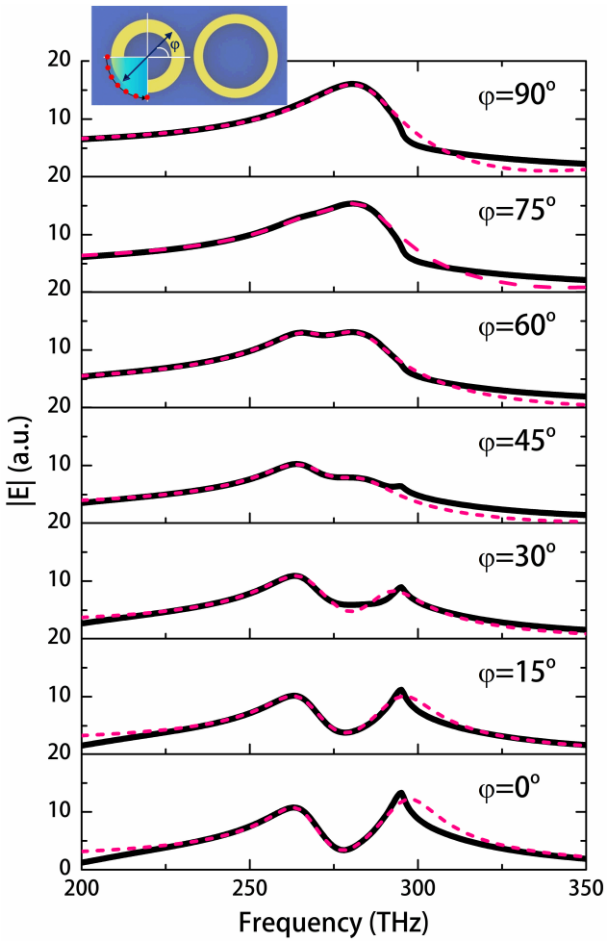

Fig. S7 Fit curves (dashed lines) of the coupled oscillator model to the simulated magnitude of the electric fields (solid lines) extracted from the field nodes of the dipolar mode illuminated under different polarizations. Red dots inset denote the extraction locations of the electric fields.

7. The coupled Lorentz oscillator model and parameters fitting

In the main text, it is discussed that, the overlap of antinodes of electric field of two modes can be tuned by rotating the polarization of incident light. The coupling strength increases owing to a larger

field overlap. According to the reviewer's suggestion, an initiative model is derived to explain the linear dependence of coupling strength on the polarization.

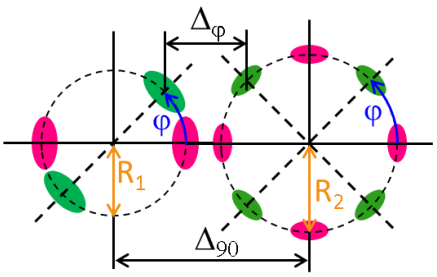

Fig. S8 Schematic of field node rotating as polarization angle varying. After polarization rotates, the field nodes rotate accordingly from positions indicated by red and green ellipses.

It is well known that the field of localized plasmon decay exponentially away from the nanostructure. In order to investigate the coupling strength between two modes, an effective length (Opt. Express, 14, 1957 (2006)) is defined to estimate the field size of dipolar mode and quadrupolar mode. As indicated in Fig. S8, these ellipses represent the effective area of field intensity antinodes of two modes, where red and green ellipses correspond to field distributions at polarization angle 0^o and φ, respectively.

As an approximation, the separation between two proximate field antinodes can be expressed as

$$\Delta_\varphi \approx \Delta_{90} - (R_1 + R_2)\cos\varphi\,. \tag{1}$$

In a linear system, it can assume that the coupling strength κ is linearly proportional to the separation between field antinodes of two modes, i.e. $\kappa(\varphi) = m\Delta_\varphi + n$, where m and n are constants determined by the system.

When $\varphi = 90^o$, the coupling between two modes is negligible. Thus

$$\kappa(90^o) = m\Delta_{90} + n = 0. \tag{2}$$

When $\varphi = 0^o$, $\Delta_0 \approx \Delta_{90} - (R_1 + R_2)$. The maximum coupling strength is

$$\kappa(0^o) = m[\Delta_{90} - (R_1 + R_2)] + n = -m(R_1 + R_2)\,. \tag{3}$$

Therefore, by inputting eqns. (2) and (3) into the definition of coupling strength, we obtain

$$\kappa(\varphi) \approx \kappa(0^o)\cos\varphi\,. \tag{4}$$

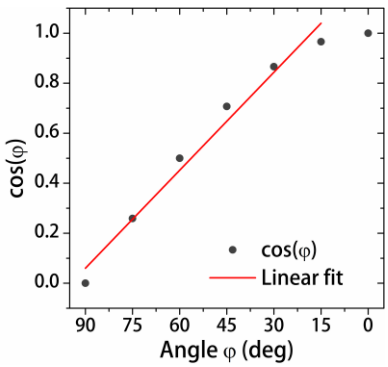

Fig. S9 Cosine function against angle. The red line is calculated by linearly fitting the first six dots.

The coupling strength of two modes, relying on the field overlap, could be well captured by our estimation. Approximately, the coupling strength is linearly proportional to the polarization angle in a large angle range.

References

1. P. B. Johnson and R. W. Christy, *Phys. Rev. B*, 1972, **6**, 4370-4379.
2. S. Zhang, D. A. Genov, Y. Wang, M. Liu and X. Zhang, *Phys. Rev. Lett.*, 2008, **101**, 047401.
3. N. Liu, L. Langguth, T. Weiss, J. Kastel, M. Fleischhauer, T. Pfau and H. Giessen, *Nat. Mater.*, 2009, **8**, 758-762.
4. S. Zhang, Z. Ye, Y. Wang, Y. Park, G. Bartal, M. Mrejen, X. Yin and X. Zhang, *Phys. Rev. Lett.*, 2012, **109**, 193902.
5. C. Ropers, D. J. Park, G. Stibenz, G. Steinmeyer, J. Kim, D. S. Kim and C. Lienau, *Phys. Rev. Lett.*, 2005, **94**, 113901.
6. A. Christ, Y. Ekinci, H. H. Solak, N. A. Gippius, S. G. Tikhodeev and O. J. F. Martin, *Phys. Rev. B*, 2007, **76**, 201405.
7. Z. Li, S. Zhang, L. Tong, P. Wang, B. Dong and H. Xu, *ACS Nano*, 2013, **8**, 701-708.